Axial Atmospheric Angular Momentum Budget at Diurnal and Subdiurnal Periodicities

FRANÇOIS LOTT
LMD/IPSL CNRS, Ecole Normale Supérieure, Paris, France

OLIVIER DE VIRON
Institut de Physique du Globe, Paris, France

PEDRO VITERBO*
European Centre for Medium-Range Weather Forecasts, Reading, United Kingdom

FRANÇOIS VIAL
LMD/IPSL CNRS, Ecole Polytechnique, Palaiseau, France

(Manuscript received 18 May 2006, in final form 23 April 2007)

ABSTRACT

The diurnal and subdiurnal variations of the mass and wind terms of the axial atmospheric angular momentum (AAM) are explored using a 1-yr integration of the Laboratoire de Météorologie Dynamique (LMDz) GCM, twelve 10-day ECMWF forecasts, and some ECMWF analysis products. In these datasets, the wind and mass AAMs present diurnal and semidiurnal oscillations for which tendencies far exceed the total torque.

In the LMDz GCM, these diurnal and semidiurnal oscillations are associated with axisymmetric ($s = 0$) and barotropic circulation modes that resemble the second gravest ($n = 2$) eigensolution of Laplace's tidal equations. This mode induces a Coriolis conversion from the wind AAM toward the mass AAM that far exceeds the total torque. At the semidiurnal period, this mode dominates the axisymmetric and barotropic circulation. At the diurnal period, this $n = 2$ mode is also present, but the barotropic circulation also presents a mode resembling the first gravest $n = 1$ eigensolution of the tidal equations. This last mode does not produce anomalies in the mass and wind AAMs.

A shallow-water axisymmetric model driven by zonal mean zonal forces, for which the vertical integral equals the zonal mean zonal stresses issued from the GCM, is then used to interpret these results. This model reproduces well the semidiurnal oscillations in mass and wind AAM, and the semidiurnal mode resembling the $n = 2$ eigensolution that produces them, when the forcing is distributed barotropically in the vertical direction. This model also reproduces diurnal modes resembling the $n = 1$ and $n = 2$ eigensolutions when the forcings are distributed more baroclinically. Among the dynamical forcings that produce these modes of motion, it is found that the mountain forcing and the divergence of the AAM flux are equally important and are more efficient than the boundary layer friction.

In geodesy, the large but opposite signals in the mass and wind AAM due to the $n = 2$ modes can lead to large errors in the evaluation of the AAM budget. The $n = 2$ responses in surface pressure can affect the earth ellipcity, and the $n = 1$ diurnal response can affect the geocenter position. For the surface pressure tide, the results suggest that the dynamical forcings of the zonal-mean zonal flow are a potential cause for its $s = 0$ component.

1. Introduction

Over the last four decades, the budget of atmospheric angular momentum (AAM) has been the subject of many studies. For geodesists, this interest follows that, for nearly all periodicities, changes in AAM correspond to changes in the parameters of the earth's rotation (Barnes et al. 1983). For climatologists, this

* Current affiliation: Instituto de Meteorologia/Instituto D. Luìs, Lisbon, Portugal.

Corresponding author address: Dr. François Lott, LMD/IPSL CNRS, Ecole Normale Supérieure, 24 rue Lhomond, 75231 Paris CEDEX 05, France.
E-mail: flott@lmd.ens.fr

DOI: 10.1175/2007JAS2178.1

interest follows that the AAM varies with planetary-scale tropical oscillations affecting the climate at intraseasonal (Madden 1987; Hendon 1995) and interannual (Chao 1984) time scales. In the extratropics and at shorter time scales it also varies with traveling Rossby waves (Lejenäs and Madden 2000), low-frequency oscillations (Lott et al. 2001, 2004a), weather regimes (Lott et al. 2004b), and synoptic-scale eddies (Iskenderian and Salstein 1998).

Although early papers revealed substantial links between observed changes in AAM and changes in the frictional torque associated with the large-scale variability of the deep convection in the tropics (Madden 1987), it is now clear that at periodicities below 40 days the mountain torque dominates the friction torque. Although the relative importance of those two torques has been debated during the 1990s (see, e.g., Weickmann et al. 1997), less attention has been paid to the relative importance of the mass angular momentum and of the wind angular momentum to the total angular momentum itself. This follows from the fact that the mass AAM contributes little to the total AAM at long periods, where most of the AAM variance is contained. Nevertheless, at periodicities below 25 days, the variations in mass AAM compare with those in wind AAM. This equipartition occurs because in this frequency band (i) the total torque is dominated by the mountain torque, (ii) the major mountain ranges are located in midlatitudes so that the mountain torque is essentially due to a mountain stress applied to the atmosphere in the midlatitudes, and (iii) the atmospheric response to this stress is in geostrophic balance (see Lott and d'Andrea 2005). This process results in lead–lag relationships between the mountain torque and the mass AAM, which have some interest for the low-frequency variability in the Northern Hemisphere extratropics (Lott et al. 2004a). Indeed, the leading mode of variability there, the Arctic Oscillation (Thompson and Wallace 1998), corresponds to a redistribution of mass from polar latitudes to the midlatitudes and the subtropics. Its variations are associated with substantial changes in mass AAM (von Storch 1999, 2001). Note, nevertheless, that Lott and d'Andrea (2005) do not discuss the fact that the mountain stress can be transmitted to the zonal flow at a long distance from the mountains that produce it.

To interpret dynamically the partition between the mass and the wind AAM in the National Centers for Environmental Prediction (NCEP) reanalysis data, Lott and d'Andrea (2005) also used an axisymmetric shallow-water model and analyzed its balanced response. Incidentally, they also found that, when the mountain torque varies abruptly (i.e., with a time scale near one day) and results in a force applied to the atmosphere in the midlatitudes, it produces wind and mass AAM oscillations with periods between 12 and 24 h. These oscillations are related to global-scale free inertio–gravity modes with zero zonal wavenumber ($s = 0$: Longuet-Higgins 1968, hereafter LH68; Tanaka and Kasahara 1992) produced in the midlatitudes during the geostrophic adjustment of the model to the torque. Note that Egger (2003) also discussed the global adjustment to mountain forcing in the context of the AAM budget.

In the real atmosphere, these modes can influence the AAM budget at diurnal and subdiurnal periodicities. Indeed, as the surface pressure fields associated with the traveling atmospheric tides vary in longitude, they result in a zonal-mean surface stress when zonal pressure gradients are pronounced over the major mountain ranges. Note that these pressure gradients can also be enhanced locally through a dynamical interaction between the traveling tidal signals and the mountains (Frei and Davies 1993). The daily cycle of the zonal-mean zonal forces on the atmosphere resulting from these interactions between the traveling tides and the mountains can trigger secondary tides with zero zonal wavenumber that give substantial but largely compensating daily fluctuations of the wind and mass AAMs.

These issues have two potential applications. The first concerns the evaluation of the earth orientation parameters. Today, the major technical problems in this context are in closing the AAM budget at daily time scales (De Viron et al. 2005): the presence of the large canceling terms presented in this paper is probably at the origin of these problems. The second concerns the dynamics of atmospheric tides. Indeed, our interpretation of the mass and wind AAM oscillations involve tidal modes generated by dynamical forcings, which have not been studied before.

The first objective of this paper is to point out that the mass and wind terms of the axial AAM budget present daily oscillations that have no substantial impact on the total AAM itself. The second objective is to describe the zonal mean and barotropic tidal patterns associated with these oscillations. The third objective is to show that these daily oscillations are in part forced by the daily cycle of the zonal forces acting on the atmosphere.

The plan of the paper is as follows. Section 2 presents the Laboratoire de Météorologie Dynamique (LMDz) General Circulation Model (GCM) used, some diagnostic equations for the zonal mean and barotropic flow evolution, the AAM budget in the LMDz GCM, and the evolutions of the mass and wind AAMs in the

LMDz GCM as well in the European Centre for Medium-Range Weather Forecasts (ECMWF) forecasts and analyses. Section 3 describes the zonal mean and barotropic flow fields associated with the semidiurnal and the diurnal motion in the LMDz GCM. Their structure is compared to the gravest axisymmetric eigensolutions of the Laplace tidal equations presented in LH68. The dynamical relationship between these fields and the semidiurnal and diurnal variations of the mass and wind AAM is also presented. Section 4 proposes a dynamical interpretation for the origin of these planetary-scale modes of motion, and for the oscillations between the mass and wind AAM. It is based on a shallow-water axisymmetric model driven by zonal forces for which the vertical integral equals the various stresses issued from the GCM. Section 5 summarizes and discusses the significance of our results for geodesy and for the atmospheric tides.

2. AAM budget in general circulation models

a. Description of the LMDz GCM simulations

The model data are derived from a 15-month simulation using the LMDz GCM at 2.5° × 2.5° horizontal resolution. The model has 19 vertical levels, with a near-uniform 2-km resolution in the middle troposphere, up to $z = 21$ km: The resolution rapidly degrades aloft, and the model has only four levels between 25 and 40 km (the model top). At the lower boundary, the model is forced by sea surface temperature and sea ice cover that varies along a climatological annual cycle deduced from monthly mean data. The solar shortwave forcing of the model takes into account both annual and daily cycles. For a more complete description of the LMDz GCM, see Hourdin et al. (2006) and Lott et al. (2005a).

The simulation starts from initial fields interpolated from the ECMWF reanalysis. To avoid spinup problems, we use only the last 12 months (i.e., one model year beginning on 1 January). During this year, instantaneous values of the two dimensional fields of surface pressure P_s, barotropic winds, meridional flux of zonal momentum, and the subgrid-scale surface stresses are stored every 30 minutes. Finally, it is important to recall that the LMDz GCM closes well the AAM budget (Lott et al. 2005b; DeViron et al. 2005) and has realistic tides [for the surface pressure P_s and for the barotropic winds, see DeViron et al. (2005)].

b. Zonal mean and AAM budget equations

The conservation law for the axial AAM can be derived by successive spatial integrations of the laws for the local evolution of the zonal wind and density. If we first limit these integrations to vertical and zonal averages, then we obtain

$$\frac{\partial \mathcal{U}}{\partial t} - 2\Omega \sin\phi \mathcal{V} = \mathcal{T} + \mathcal{F} + \mathcal{B}, \tag{1}$$

$$\frac{\partial \mathcal{M}}{\partial t} + \frac{1}{r\cos\phi}\frac{\partial}{\partial \phi}\cos\phi \mathcal{V} = 0. \tag{2}$$

Here Ω is the earth's rate of rotation, ϕ is latitude, and r the earth's radius. In Eqs. (1) and (2) $\mathcal{M}$ is the zonal mean of the atmospheric mass per unit area, while $\mathcal{U}$ and $\mathcal{V}$ are the zonal mean of the barotropic zonal and meridional momentum per unit area, respectively:

$$\mathcal{M} = \frac{1}{2\pi}\int_0^{2\pi}\frac{P_s}{g}\,d\lambda, \quad \mathcal{U} = \frac{1}{2\pi}\int_0^{2\pi}\int_0^{Ps} u\,\frac{dp}{g}\,d\lambda,$$

$$\mathcal{V} = \frac{1}{2\pi}\int_0^{2\pi}\int_0^{Ps} v\,\frac{dp}{g}\,d\lambda. \tag{3}$$

Here p is pressure, g the gravity constant, λ is longitude, and $u(v)$ the zonal (meridional) wind. The forcing terms $\mathcal{F}$, $\mathcal{B}$, and $\mathcal{T}$ in Eq. (1) are given by

$$\mathcal{F} = -\frac{1}{r\cos^2\phi}\frac{\partial}{\partial\phi}\frac{\cos^2\phi}{2\pi}\int_0^{2\pi}\int_0^{Ps} uv\,\frac{dp}{g}\,d\lambda,$$

$$\mathcal{B} = \frac{1}{2\pi}\int_0^{2\pi}\tau_B\,d\lambda, \quad \mathcal{T} = -\frac{1}{2\pi}\frac{1}{r\cos\phi}\int_0^{2\pi} P_s\frac{\partial Z_s}{\partial\lambda}\,d\lambda. \tag{4}$$

Here Z_s is the ground level elevation and τ_B is the subgrid-scale surface friction. More specifically, these forcings are the divergence of the angular momentum flux ($\mathcal{F}$), the surface stress associated with the explicit longitudinal pressure differences across mountains ($\mathcal{T}$), and the zonal mean of the parameterized surface stresses ($\mathcal{B}$). In this formalism, the global AAM tendency is given by

$$\frac{dM}{dt} = T, \tag{5}$$

where $M = M_O + M_R$ and $T = T_M + T_B$; M is the absolute AAM, M_O is the mass AAM, and M_R is the wind AAM:

$$M_O = 2\pi r^4\Omega\int_{-\pi/2}^{\pi/2}\cos^3\phi\mathcal{M}\,d\phi,$$

$$M_R = 2\pi r^3\int_{-\pi/2}^{\pi/2}\cos^2\phi\mathcal{U}\,d\phi. \tag{6}$$

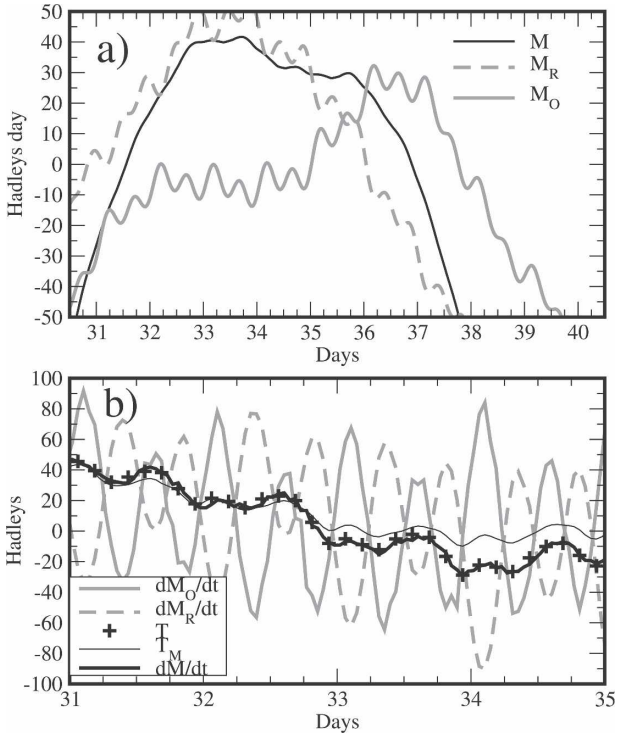

FIG. 1. (a) The AAM budget, in the LMDz GCM for the first 10 days of February: total AAM (M, black solid), mass AAM (M_O, gray solid), and wind AAM (M_r, gray dashed). For clarity, each curve has been shifted vertically. (b) As in (a) but for the first 5 days of February: global AAM tendency (dM/dt, thick black solid), mass AAM tendency (dM_O/dt, gray solid), wind AAM tendency (dM_R/dt, gray dashed), total torque (T, plus symbols), and mountain torque (T_M, thin solid).

Still, in Eq. (5) T is the total torque, T_M is the mountain torque, and T_B is the frictional torque:

$$T_M = 2\pi r^3 \int_{-\pi/2}^{\pi/2} \cos^2\phi \mathcal{T}\, d\phi,$$

$$T_B = 2\pi r^3 \int_{-\pi/2}^{\pi/2} \cos^2\phi \mathcal{B}\, d\phi. \quad (7)$$

To interpret the exchanges between M_R and M_O, it is also useful to split the AAM budget in Eq. (5) into two parts (von Storch 2001) and to introduce the Coriolis conversion term C:

$$\frac{dM_O}{dt} = C, \quad \frac{dM_R}{dt} = -C + T, \quad (8)$$

where $C = -4\pi r^3 \Omega \int_{-\pi/2}^{\pi/2} \cos^2\phi \sin\phi\, \mathcal{V}\, d\phi$.

c. AAM budget from the LMDz GCM and the ECMWF model

An example of the evolution of the AAM in the LMDz GCM is shown in Fig. 1a. We see that the absolute AAM M expressed in units of hadley day (Hd, where 1 Hd = 8.64×10^{22} kg m^2 s^{-1}) has a diurnal cycle, which is hardly visible. On the contrary, M_O and M_r present daily fluctuations reaching 10 Hd (from minima to maxima) that nearly exactly balance to give a small daily cycle in M.

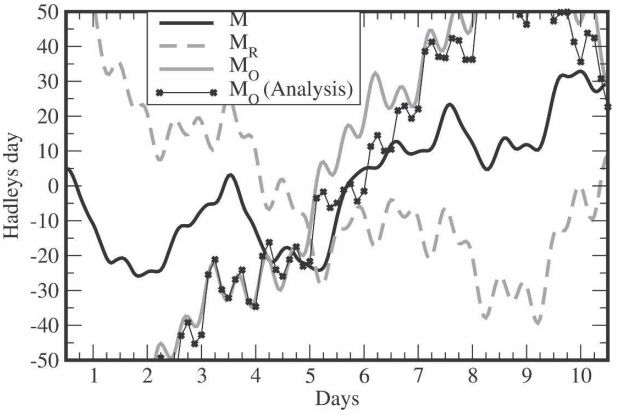

FIG. 2. The AAM in the ECMWF model, 10-day forecast starting 1 Feb 2004, and its corresponding analysis of total AAM (M: black solid), mass AAM (M_O: gray solid), wind AAM (M_r: gray dashed), and mass AAM from the analysis (solid with dots). For clarity, each curve has been shifted vertically.

The corresponding tendencies of M, M_R, and M_O are shown in Fig. 1b, which compares them to the total torque T and to the mountain torque T_M. We see that the AAM budget in Eq. (5) expressed in units of hadleys (H, where 1 H = 10^{18} kg m^2) is well closed with the tendency of M (thick solid) coinciding almost exactly with the total torque T (plus). Note also that the total torque is in large part due to the mountain torque T_M (thin solid). In particular, T presents daily oscillations with amplitude ~10 H, and which are essentially due to T_M. Note also that the two tendencies in M_O and M_R (thick gray solid and thick gray dashed) present daily fluctuations that are much more substantial and that reach 100 H.

These oscillations between the mass and the wind AAM are not specific to the LMDz GCM. This is illustrated in Fig. 2, which presents M, M_O, and M_R issued from the ECMWF 10-day forecast, starting 1 February 2004, and for which the AAM data have been provided every hour. It shows that the daily oscillations between M_R and M_O are also substantial in the ECMWF model. They compare rather well in amplitude and phase with the corresponding oscillations in the LMDz GCM (Fig. 1). It is also noticeable that the oscillations of the mass AAM that we analyze are also present in the ECMWF analysis (solid line with dots in Fig. 2). This indicates that they are not related to an initial adjustment of this model at the beginning of the fore-

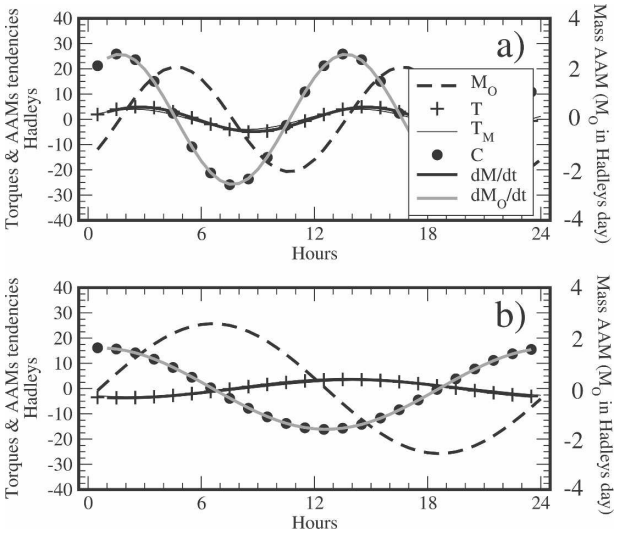

FIG. 3. Mass AAM and mass AAM budgets for (a) semidiurnal and (b) diurnal cycles: mass AAM (M_O, thick dashed), total torque (T, plus), mountain torque (T_M, thin), Coriolis conversion (C, thick dots), total AAM tendency (dM/dt, thick solid), and mass AAM tendency (dMO/dt, thick gray). Note that in (a) and (b) the thin line for T_M almost coincides with the thick line for dM/dt.

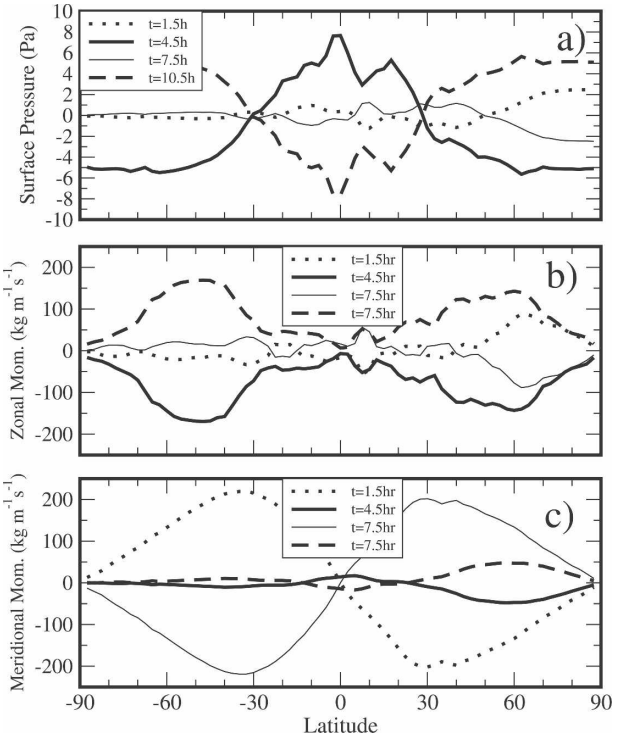

FIG. 4. Semidiurnal cycle, in the LMDz GCM, of the zonal mean and barotropic diagnostics for the zonal mean of (a) the surface pressure ($g\mathcal{M}$), (b) the barotropic zonal momentum ($\mathcal{U}$), and (c) the barotropic meridional momentum ($\mathcal{V}$).

casts and that they are somehow present in the datasets that are used to produce the analysis.

3. Tidal signals responsible for the mass and wind AAM variations

a. Methodology and application to M_O

To extract the diurnal and the subdiurnal signals from the LMDz GCM we follow a conventional procedure and first build a mean daily cycle for each quantity. For the mean daily cycle of the mass AAM, for instance, we evaluate for each 30 min of the day, the yearly average of the value of M_O at the same time. From the resulting 48-point half-hourly time series we then subtract the linear trend to ensure a perfect 24 h period. We then extract the diurnal and subdiurnal signals by applying a Fourier decomposition to this mean daily cycle.

The mean daily cycle for M_O (not shown) has an amplitude of 5–6 Hd. From minimum to maximum it corresponds to the 10-Hd mass AAM daily fluctuations that are directly apparent in Fig. 1a. The semidiurnal and the diurnal cycles for the mass AAM are shown by the thick dashed line in Figs. 3a and 3b, respectively. Their amplitudes are comparable (around 2–3 Hd for both), but their phases differ: the semidiurnal mass AAM maximum is at $t = 4.5$ h and the diurnal mass AAM maximum is at $t = 7$ h It is noticeable that the contribution of the shorter periodicities is quite small (not shown): the diurnal and the semidiurnal signals of M_O explain almost entirely the daily cycle of M_O.

To sample the mean daily cycle from the ECMWF model, we have also used 12 ECMWF 10-day forecasts starting the first day of each month during the year 2004. We have then followed the same procedure to construct a mean daily cycle and to extract the diurnal and subdiurnal signals. The results (not shown) are in good agreement with the diurnal and subdiurnal cycles from the LMDz GCM in Fig. 3.

b. Semidiurnal zonal mean diagnostics

According to Eq. (6), M_O strongly depends on the latitudinal distribution of the zonal mean mass $\mathcal{M}$. Its semidiurnal component is shown in Fig. 4a at four different times separated by one-quarter period. At $t = 4.5$ h, the pattern of $\mathcal{M}$ presents an excess of mass everywhere in the tropical band (i.e., between 30°S and 30°N) equilibrated by a deficit of mass everywhere in the midlatitude and polar regions. It is also at this time that the semidiurnal component of M_O is maximum (Fig. 3a), and this is due to the fact that the atmospheric masses have been moved away from the earth's rotation axis. At all times, the patterns for $\mathcal{M}$ are also rather

smooth and resemble the geopotential height of the axisymmetric ($s = 0$) eigensolution of the Laplace tidal equations with $n = 2$ nodes between the poles (see LH68, Fig. 7). Furthermore, the location of the nodes at $\phi \approx \pm 30°$ in Fig. 4a indicate that the Lamb parameter

$$\gamma = \frac{4\Omega^2 r^2}{gH_0},$$

of the $n = 2$ eigensolution in LH68 that fits the best the patterns of $\mathcal{M}$ is near $\gamma \approx 10$. Here H_0 is an equivalent depth associated with the vertical structure of the tidal signal associated with $\mathcal{M}$ [see Chapman and Lindzen (1970) and section 4 below].

The semidiurnal signal for $\mathcal{U}$ is shown in Fig. 4b. It is everywhere negative at $t = 4.5$ h, thus yielding a negative M_R (not shown). This pattern for $\mathcal{U}$ is also smooth, with minima at $t = 4.5$ h located around $\phi = \pm 50°$. This again resembles to the zonal wind signal associated with the $n = 2$, $\gamma \approx 10$ eigensolution shown in LH68 (their Fig. 7). The semidiurnal signal for $\mathcal{V}$ is shown in Fig. 4c; it is antisymmetric with respect to the equator with only 1 node between the poles. It also resembles to the meridional wind pattern associated with the $n = 2$, $\gamma \approx 10$ eigensolution in LH68 (their Fig. 7).

It is noticeable that $\mathcal{V}$ is in temporal quadrature with both $\mathcal{M}$ and $\mathcal{U}$. For $\mathcal{M}$ it follows that $\mathcal{V}$ moves mass in the latitudinal direction according to the mass conservation in Eq. (2): in quadrature before $\mathcal{M}$ is maximum in the equatorial region, $\mathcal{V}$ is large and positive in the Southern Hemisphere and large and negative in the Northern Hemisphere (at $t = 1.5$ h in Fig. 4c), producing a convergence of mass toward the equatorial band. If we return to the budget for M_O in Fig. 3a, we also see that this pattern for $\mathcal{V}$ produces a maximum of the Coriolis conversion term C at $t = 1.5$ h (dots in Fig. 3a). Notably, the Coriolis conversion is one order of magnitude larger than the torques (thin solid for T_M and plus for T), which explains why the variations in M_O (thick gray) are one order of magnitude larger than those for M (thick black).

Note also that the displacement toward the equator associated with $\mathcal{V}$ at $t = 1.5$ h in Fig. 4c produces negative tendencies for $\mathcal{U}$ via the Coriolis torque, implying that $\mathcal{U} < 0$ almost everywhere a quarter of cycle later (at $t = 4.5$ h in Fig. 4b). Nevertheless, this last argument is only valid if the Coriolis torque dominates the other forcings of the barotropic zonal wind tendency $\partial_t \mathcal{U}$ in Eq. (1). This is confirmed in Fig. 5, which shows that at $t = 1.5$ h the Coriolis term (thick gray) almost opposes the $\mathcal{U}$ tendency (thick black). Both are much larger than the sum of the three forcings $\mathcal{F} + \mathcal{T} + \mathcal{B}$ (dots in Fig. 5a): their sum (thin line in Fig. 5a) equals $\mathcal{F} + \mathcal{T} + \mathcal{B}$ almost exactly.

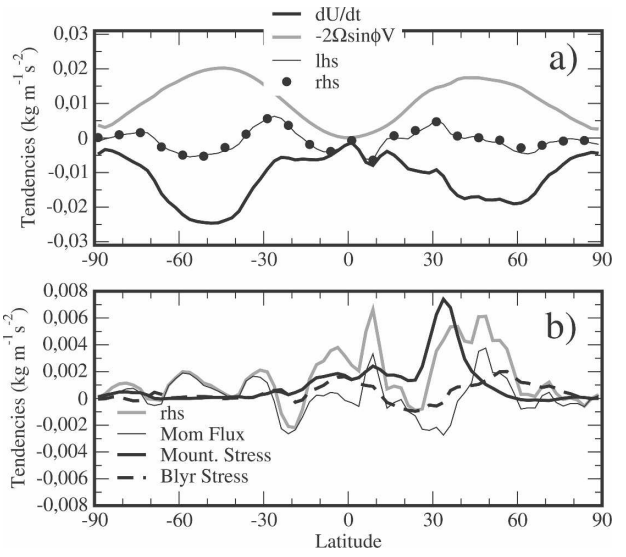

FIG. 5. Zonal mean barotropic momentum budget, Eqs. (1) and (2), showing semidiurnal signals (a) at $t = 1.5$ h of the zonal momentum tendency ($\partial_t \mathcal{U}$, thick solid), Coriolis term ($-2\Omega \sin\phi \mathcal{V}$, thick gray solid), and lhs (thin) and rhs (dots) of Eq. (1) and, (b) at $t = 2.5$ h of lhs of Eq. (1) (thick gray solid) of the momentum flux divergence ($\mathcal{F}$, thin solid), mountain stress ($\mathcal{T}$, thick black), and boundary layer stress ($\mathcal{B}$, thick black dashed line).

In the context of this budget, Fig. 5b compares the three forcing terms, $\mathcal{F}$, $\mathcal{T}$, and $\mathcal{B}$ at $t = 2.5$ h. At this time, the semidiurnal mountain torque T_M (thin line in Fig. 3a) is at a maximum and the mountain stress $\mathcal{T}$ is positive everywhere, with a pronounced maximum in the Northern Hemisphere at $\phi \approx 35°$N (thick solid). At this time, the boundary layer stress $\mathcal{B}$ is substantially smaller than $\mathcal{T}$ (thick dashed) and never becomes substantially larger than at other times (not shown). Although it does not produce a global torque, the momentum flux divergence is also shown in Fig. 5b. Clearly, it induces a redistribution of the angular momentum in latitude, which is locally comparable in amplitude with the effect of the mountain stress $\mathcal{T}$.

c. *Diurnal zonal mean diagnostics*

The diurnal components for $\mathcal{M}$, $\mathcal{U}$, and $\mathcal{V}$ are more complex than the semidiurnal components. To clarify their description, we will next split each of them into two parts that are symmetric and antisymmetric with respect to the equator.

The antisymmetric part of $\mathcal{M}$ is shown in Fig. 6a. The first time shown ($t = 5$ h, thick solid line) is also the time at which $\mathcal{M}$ reaches its maximum value in the Northern Hemisphere. This pattern is clearly dominated by a planetary-scale structure in which the entire mass in one hemisphere opposes that in the other. Its structure resembles the height pattern associated with

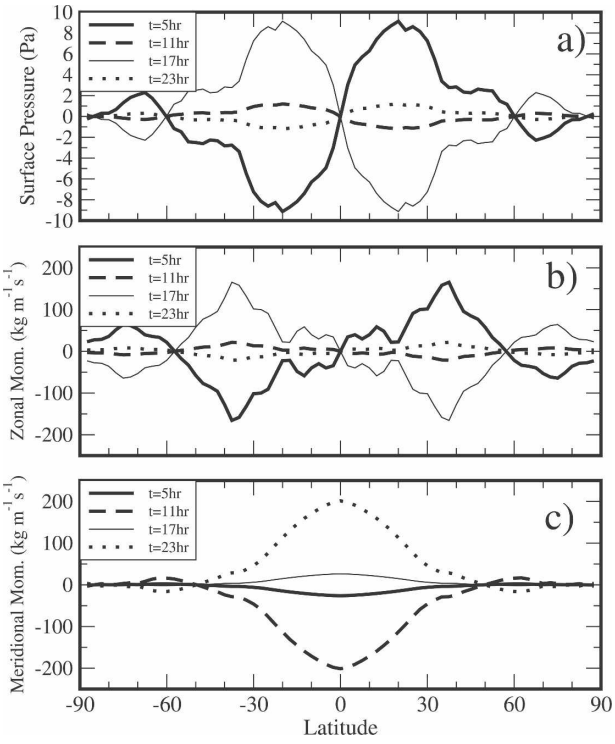

FIG. 6. Diurnal cycle, in the LMDz GCM, for zonal mean and barotropic diagnostics of the zonal mean of (a) the surface pressure ($g\mathcal{M}$) pattern antisymmetric with respect to the equator, (b) the barotropic zonal momentum ($\mathcal{U}$) pattern antisymmetric with respect to the equator, and (c) the barotropic meridional momentum ($\mathcal{V}$) pattern symmetric with respect to the equator.

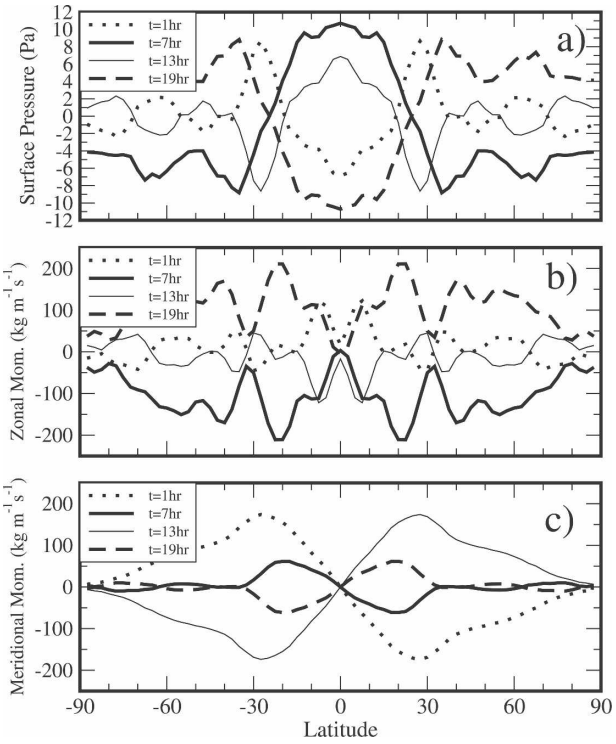

FIG. 7. As in Fig. 6 but for (a) the $g\mathcal{M}$ pattern symmetric, (b) the $\mathcal{U}$ pattern symmetric, and (c) the $\mathcal{V}$ pattern antisymmetric with respect to the equator.

the $n = 1$, $s = 0$ eigensolution of the Laplace tidal equations (Fig. 7 in LH68). Note that the anomalies in mass in Fig. 6a are not very pronounced in the polar regions and have maxima around $\pm 20°$, suggesting a value for the Lamb parameter $\gamma \approx 100$ (see again Fig. 7 in LH68). The antisymmetric patterns of $\mathcal{U}$ in Fig. 6b grossly corroborate those for $\mathcal{M}$: they resemble the zonal wind structure of the $n = 1$ eigensolution in LH68. As the eigensolutions that are antisymmetric in geopotential height and zonal wind are symmetric in meridional wind, Fig. 6c shows the diurnal signal of the symmetric part of $\mathcal{V}$. At a given time, the sign of $\mathcal{V}$ is almost independent of latitude and $\mathcal{V}$ has one well-defined maximum at the equator. It thus exchanges mass from one hemisphere to the other. Note also that for $\mathcal{V}$ the resemblance with the $n = 1$, $\gamma \approx 100$ eigensolution in LH68 is the best.

It is noticeable that this antisymmetric part of the diurnal signal of $\mathcal{M}$ moves mass from one hemisphere to the other. It does not produce M_0 anomalies because it does not move the mass away from the earth's rotation axis. Similarly, the equatorial antisymmetric part of $\mathcal{U}$ in Fig. 6b does not affect the wind AAM. In agreement with these results, the symmetric patterns for $\mathcal{V}$ in Fig. 6c results in a Coriolis conversion term [C in Eq. (8)] that is exactly null.

The symmetric part of the diurnal signal of $\mathcal{M}$ is shown in Fig. 7a. The thick solid line at $t = 7$ h is also the time at which $\mathcal{M}$ is largest in the equatorial band. By its shape, this pattern resembles the geopotential signal associated with the $n = 2$ eigensolution of the tidal equations. By comparison with LH68, the latitudinal structure of $\mathcal{M}$ in Fig. 7a suggests a value for the Lamb parameter again near $\gamma \approx 100$. For $\mathcal{U}$ in Fig. 7b, the resemblance with the zonal wind of the $n = 2$ eigensolution is quite difficult to establish because $\mathcal{U}$ is quite irregular. Nevertheless, note that $\mathcal{U}$ is negative at all latitudes when $\mathcal{M}$ is positive in the equatorial band, a property in common with the zonal wind of the $n = 2$ eigensolution in LH68. Finally the antisymmetric pattern for the diurnal signal of $\mathcal{V}$ is shown in Fig. 7c. Its shape is rather smooth, and the resemblance with the meridional wind associated with the $n = 2$ eigensolution is rather good.

The fact that the patterns for $\mathcal{V}$ in Fig. 7c are rather smooth while those for $\mathcal{U}$ in Fig. 7b are much more irregular implies that, in the evolution for $\mathcal{U}$ in Eq. (1), the role of the Coriolis force is not as prominent as it is

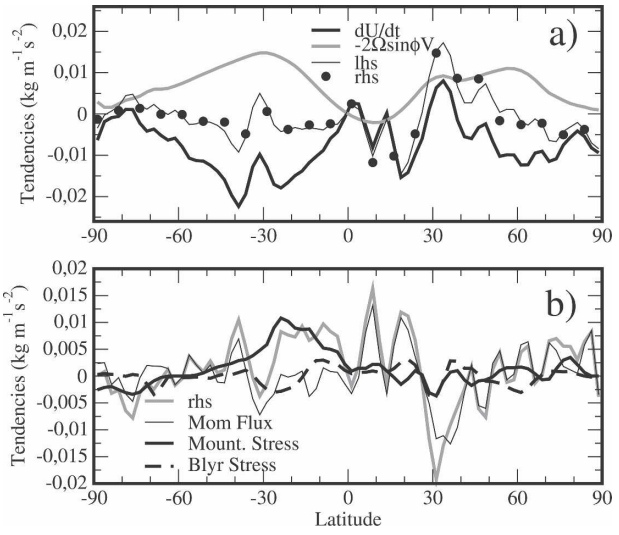

FIG. 8. Zonal mean barotropic momentum budget, Eqs. (1) and (2), showing diurnal signals (a) at $t = 1$ h of the zonal momentum tendency ($\partial_t \mathcal{U}$, thick solid), Coriolis term ($-2\Omega\sin\varphi\mathcal{V}$, thick gray solid), lhs (thin) and rhs (dots) of Eq. (1), and (b) at $t = 13$ h of the lhs of Eq. (1) (thick gray solid), momentum flux divergence ($\mathcal{F}$, thin solid), mountain stress ($\mathcal{T}$, thick black), and boundary layer stress ($\mathcal{B}$, thick black dashed).

in the semidiurnal case. This point is illustrated in Fig. 8a, which shows that at $t = 1$ h the forcing term in the lhs of Eq. (1) (thin solid) can become larger than the Coriolis term (thick gray). At this time, this forcing is particularly pronounced around latitude $\phi = 30°$N where it is in good part equilibrated by the tendency for the zonal-mean barotropic zonal wind $\mathcal{U}$ (thick solid) rather than by the Coriolis term (thick gray).

To establish more precisely which among the three forcings ($\mathcal{F}$, $\mathcal{T}$, or $\mathcal{B}$) is producing the irregular patterns in $\mathcal{U}$, Fig. 8b compares $\mathcal{F}$, $\mathcal{T}$, and $\mathcal{B}$ at $t = 13$ h. At this time, the diurnal mountain torque is at a maximum (thin line in Fig. 3b), and the mountain stress $\mathcal{T}$ presents a broad maximum in the Southern Hemisphere subtropics (thick line in Fig. 8b). At the same time, the divergence of the momentum flux $\mathcal{F}$ (thin line in Fig. 8b) presents a pronounced minimum in the NH midlatitudes, which has amplitude twice that of the maximum value of $\mathcal{T}$. Here $\mathcal{F}$ is also much more irregular than $\mathcal{T}$, and this stays valid at other times (including at $t = 1$ h as in Fig. 8a, not shown). Accordingly, it is likely that the irregular structures of the $\mathcal{U}$ field in Fig. 7b are in good part related to the forcing by the angular momentum flux divergence.

The AAM budgets associated with the diurnal patterns in Fig. 7 are shown in Fig. 3b. In it, we see that the $\mathcal{V}$ pattern at $t = 1$ h is almost at a maximum of the Coriolis conversion terms C (dots in Fig. 3b). Here again, note that the Coriolis conversion term C is one order of magnitude larger than the total torque T.

4. Interpretation with a shallow-water model

a. Model description and experimental setup

The fact that the barotropic zonal mean flow responsible for the large daily fluctuations in M_R and M_O resembles the eigensolutions of the shallow-water equations suggests that the stresses in the lhs of Eq. (1) are associated with zonal-mean zonal forces that trigger these resonant modes of motion. To illustrate how this can occur, we consider a simplified model where a zonally symmetric atmosphere responds to a small zonal-mean dynamical forcing $\overline{X}$. If we assume an atmosphere that is isothermal at rest, the response to $\overline{X}$ can be described using the hydrostatic linear set of equations:

$$\rho_0 \frac{\partial \overline{u}}{\partial t} - 2\Omega \sin\phi \rho_0 \overline{v} = \overline{X}, \tag{9}$$

$$\rho_0 \frac{\partial \overline{v}}{\partial t} + 2\Omega \sin\phi \rho_0 \overline{u} = -\frac{g}{r}\frac{\partial \overline{h}}{\partial \phi}, \tag{10}$$

$$\frac{\partial}{\partial t}\left(\frac{\partial \overline{h}}{\partial z} + (1-\kappa)\frac{\overline{h}}{H}\right) + \frac{\kappa}{H}\rho_0 \overline{w} = 0, \tag{11}$$

$$\frac{\partial}{\partial t}\frac{\partial \overline{h}}{\partial z} - \frac{1}{r\cos\phi}\frac{\partial}{\partial \phi}\cos\phi \rho_0 \overline{v} - \frac{\partial}{\partial z}\rho_0 \overline{w} = 0. \tag{12}$$

In Eqs. (9)–(12), $\overline{u}$, $\overline{v}$, and $\overline{w}$ are the three components of the zonal mean wind, $\rho_0 = \exp(-z/H)$ is a nondimensional profile for the basic density, and H is the mean scale height $H = RT_r/g$ (where T_r is the temperature of the atmosphere at rest and R is the gas constant for dry air). Finally, $\kappa = R/c_p = 2/7$ in which c_p is the specific heat at constant pressure, and the zonal mean pressure has been written $\overline{p} = \rho_r g \overline{h}$, where $\rho_r = 1$ kg m^{-3} is a constant reference density.

If we now assume that the forcing function is separable in the vertical direction and can be written

$$\overline{X} = \tilde{X}(t, \phi)\exp(-z/2H - \beta z), \tag{13}$$

where $\tilde{X}$ is a real function, a particular solution to the set of Eqs. (9)–(12) can be searched in the form

$$(\rho_0\overline{u}, \rho_0\overline{v}, \rho_0\overline{w}, \overline{h}) = (\tilde{u}, \tilde{v}, \tilde{w}, \tilde{h})(t, \phi)\exp(-z/2H - \beta z). \tag{14}$$

After substitution, this yields to the linearized shallow-water system:

$$\frac{\partial \tilde{u}}{\partial t} - 2\Omega \sin\phi \tilde{v} = \tilde{X}, \tag{15}$$

$$\frac{\partial \tilde{v}}{\partial t} + 2\Omega \sin\phi \tilde{u} = -\frac{g}{r}\frac{\partial \tilde{h}}{\partial \phi}, \tag{16}$$

$$\frac{\partial \tilde{h}}{\partial t} + \frac{H_0}{r\cos\phi}\frac{\partial}{\partial \phi}\cos\phi \tilde{v} = 0, \tag{17}$$

where H_0 is the equivalent depth:

$$H_0 = \frac{\kappa H}{¼ - \beta^2 H^2}. \tag{18}$$

When $\tilde{X} = 0$, Eqs. (15)–(17) are the equations for the tides with zonal wavenumber zero (LH68).

To analyze the response to the forcing $\tilde{X}$ we solve the shallow-water set of Eqs. (15)–(16) with the finite difference model described in Lott and d'Andrea (2005). To specify $\tilde{X}$ we take from the GCM the semidiurnal and the diurnal cycles of the stresses $\mathcal{F}$, $\mathcal{T}$, and $\mathcal{B}$ in Eq. (4) (see also Figs. 5b and 8b) and equal each of them to the stress due to $\overline{X}$ in Eq. (9). More specifically, and to mimic the mountain forcing for instance, we evaluate the surface stress associated with the zonal force $\overline{X}$ and equal it to $\mathcal{T}$:

$$\int_0^\infty \rho_r \overline{X}\, dz = \frac{\rho_r \tilde{X}}{½H + \beta} = \mathcal{T}. \tag{19}$$

Using Eq. (13), this yields to $\tilde{X} = \mathcal{T}/\rho_r H_0$ in the barotropic case in section 4b, and $\tilde{X} = 2\kappa\mathcal{T}/\rho_r H_0$ in the baroclinic case in section 4c. Then, the shallow-water model is integrated over one year, with the amplitude of the forcing increasing smoothly and uniformly during the first six months. This reduces the influence of the spinup in the model and ensures that the period of the response at the end of the simulation is exactly that of the forcing. We then analyze the response to each forcings ($\mathcal{F}$, $\mathcal{T}$, and $\mathcal{B}$) looking at the last day of the simulations.

b. *Barotropic configuration and semidiurnal response*

If we take for the parameter β the value

$$\beta = \frac{1-\kappa}{H} - \frac{1}{2H},$$

then the equivalent depth $H_0 = H/(1 - \kappa)$ and the thermodynamic equation (11) implies that our particular solution $\overline{w} = 0$: this solution also satisfies a free-slip lower boundary condition and has the vertical structure of a Lamb wave (Lamb 1932). In this configuration Eqs. (15)–(17) satisfy the AAM budget:

$$\frac{d}{dt}(M_R + M_O) = T_X, \tag{20}$$

where the wind AAM, mass AAM, and torque due to X are

$$M_R = 2\pi r^3 \int_{-\pi/2}^{+\pi/2} \cos^2\phi \rho_r H_0 \tilde{u}\, d\phi,$$

$$M_O = 2\pi r^4 \Omega \int_{-\pi/2}^{+\pi/2} \cos^3\phi \rho_r \tilde{h}\, d\phi, \tag{21}$$

$$T_X = 2\pi r^3 \int_{-\pi/2}^{+\pi/2} \cos^2\phi \rho_r H_0 \tilde{X}\, d\phi. \tag{22}$$

This AAM budget is close to the AAM budget in Eqs. (5), replacing (i) $\mathcal{U}$ in the definition of M_R in Eq. (6) by $\rho_r H_0 \tilde{u}$, (ii) $\mathcal{M}$ in the definition of MO by $\rho_r \tilde{h}$, and (iii) the stresses ($\mathcal{F}$, $\mathcal{T}$, or $\mathcal{B}$) in the definition of the torques in Eq. (7) by $\rho_r H_0 \tilde{X}$. Similarly, a separate budget for the mass AAM can be written

$$\frac{dM_O}{dt} = C, \tag{23}$$

where $C = -4\pi r^3 \Omega \int_{-\pi/2}^{\pi/2} \cos^2\phi \sin\phi\, \rho_r H_0 \tilde{v}\, d\phi$. Here the Coriolis conversion term is as in Eq. (8) replacing $\mathcal{V}$ by $\rho_r H_0 \tilde{v}$.

The semidiurnal evolution of the AAM budget in the shallow-water model is presented in Fig. 9 when $H_0 =$ 9.5 km. When the forcing $\tilde{X}$ is keyed to the mountain stress $\mathcal{T}$, the mass AAM tendency (dM_O/dt thick gray solid) presents a semidiurnal cycle that far exceeds the corresponding cycle in the absolute AAM tendency (dM/dt thick solid). This comparatively large daily cycle is due to the fact that the Coriolis conversion term (C, black dots) far exceeds the mountain torque (T_X, plus). The corresponding amplitude of the cycle in M_O is around 2 Hd (thick gray in Fig. 9b), a value quantitatively comparable with the semidiurnal signal seen in the mass AAM from the LMDz GCM (Fig. 3a). Note also that the phase is almost correct with a maximum in M_0 at $t = 5.5$ h (Fig. 9a), while the maximum for M_O in the LMDz GCM is at $t = 4.5$ h (Fig. 3a).

To establish the significance of the other forcings, Fig. 9b shows the mass AAM cycles when $\tilde{X}$ is keyed to $\mathcal{F}$ and $\mathcal{B}$. The amplitude of the M_O response to $\mathcal{F}$ is also quite large (gray dashed in Fig. 9b), but the phase is almost in phase opposition with that found in the LMDz GCM (Fig. 3a). Finally, note that the response when the shallow-water model is keyed to $\mathcal{B}$ is significantly smaller than for the two others (gray dots in Fig.

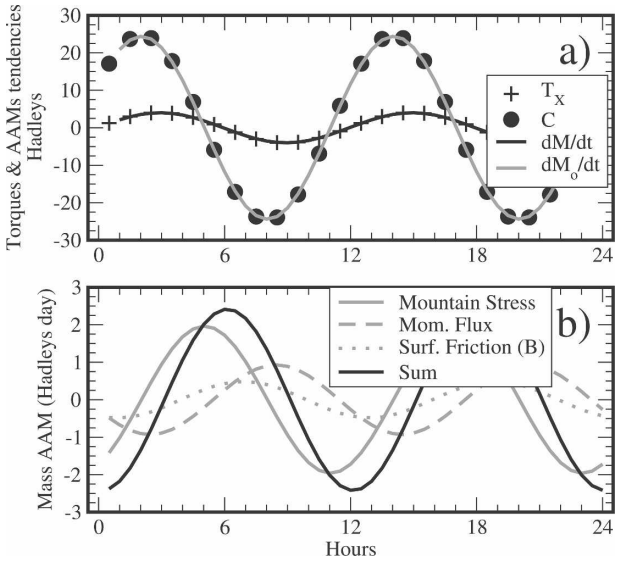

FIG. 9. Semidiurnal responses in the shallow-water model with $H_0 = 9.5$ km: (a) AAM budget when the forcing $\tilde{X}$ is keyed to the mountain stress $\mathcal{T}$ of the total AAM tendency (dM/dt, thick solid line), mass AAM tendency (dM/dt, thick gray solid), torque due to the forcing (T_X, plus symbols), and Coriolis conversion term (C, dots); (b) mass AAM cycle when $\tilde{X}$ is keyed to the various stresses in Fig. 5a of the mountain stress ($\mathcal{T}$, thick gray), momentum flux divergence ($\mathcal{F}$, thick gray dashed), boundary layer stress ($\mathcal{B}$, thick gray dots), and the sum ($\mathcal{T} + \mathcal{F} + \mathcal{B}$, thick black solid).

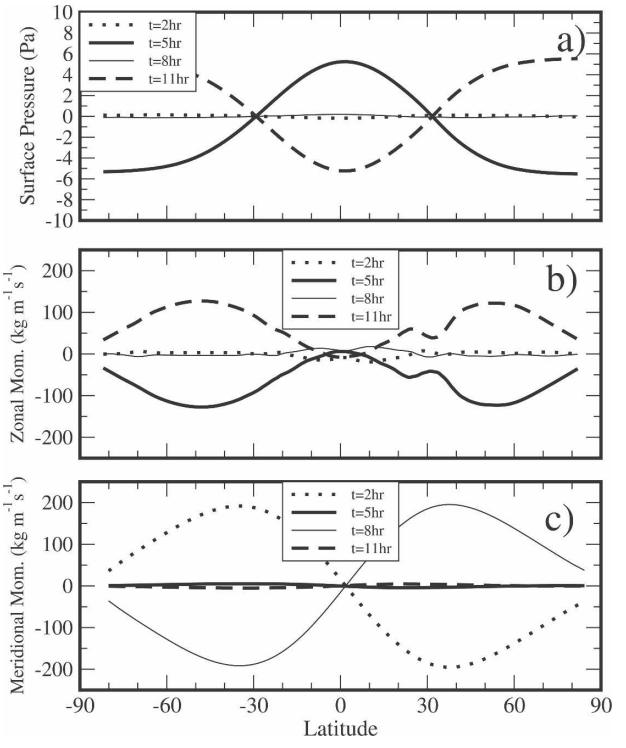

FIG. 10. Semidiurnal response for the shallow-water model with $H_0 = 9.5$ km and when $\tilde{X}$ is keyed to the mountain stress $\mathcal{T}$ of the (a) surface pressure (i.e., $\rho_r g\tilde{h}$), (b) zonal momentum (i.e., $\rho_r H_0 \tilde{u}$), and (c) meridional momentum (i.e., $\rho_r H_0 \tilde{v}$).

9b). This naturally follows that the boundary layer stress is by far the smallest stress at the semidiurnal period (Fig. 5b).

The fields $\rho_r g\tilde{h}$, $\rho_r H_0 \tilde{u}$, and $\rho_r H_0 \tilde{v}$ associated with the semidiurnal mountain stress $\mathcal{T}$ are shown in Fig. 10. As for the semidiurnal zonal mean and barotropic fields from the LMDz GCM in Fig. 4, the shallow-water model response resembles the second gravest mode ($n = 2$) eigensolution of the axisymmetric ($s = 0$) Laplace tidal equations shown in Fig. 7 of LH68. The best correspondence is with the $n = 2$ eigensolution associated with Lamb parameter $\gamma = 10$, which follows that the value $H_0 = 9.5$ km yields $\gamma \approx 9.3$. Note also that the amplitudes of all fields from the shallow-water model match relatively well the corresponding fields from the GCM in Fig. 4.

c. *Sensitivity test to the value of H_0*

To understand the shallow-water model response, it is necessary to refer to Fig. 1 from LH68, where the dispersion curves for the $s = 0$ eigensolutions of the Laplace tidal equations are shown. From this figure, we can deduce that for the semidiurnal frequency, $\sigma/2\Omega = 1$, the eigenvalues of the Lamb parameters γ_n increase with n and the values of the leading ones are given by

$$\gamma_1 \approx 3 < \gamma_2 \approx 10 < \gamma_3 \approx 25 < \cdots < \gamma_n < \gamma_{n+1} < \cdots. \tag{24}$$

When $H_0 = 9.5$ km, the Lamb parameter $\gamma = 9.3$ is near $\gamma_2 = 10$ in Eq. (24), which means that the semidiurnal forcing is in near resonance with the $n = 2$ eigenmode. Note also that the forcing is subcritical regarding this eigensolution, in the sense that the semidiurnal frequency is smaller than the period of the $n = 2$ eigensolution of the shallow-water equation.

Because of this resonant behavior, it is important to analyze the sensitivity of our result to the choice of H_0. This is done in Fig. 11, which shows the maximum amplitude and phase of the mass AAM response when the forcing $\tilde{X}$ is keyed to the semidiurnal mountain stress $\mathcal{T}$. We see that there is a large range of values for H_0 (from 9.2 to 10 km) that leads to maxima in M_0 around $M_O \approx$ 1–3 Hd: our choice for H_0 is not the one for which the resonant amplification is extremely large (i.e., around $H_0 \approx 8.9$ km). Note also that the phase (i.e., the time at which M_O reaches its maximum value) is almost insensitive to the value of H_0, as long as our forcing is subcritical. Nevertheless, note that the whole response changes sign (e.g., the time of the maximum for M_O

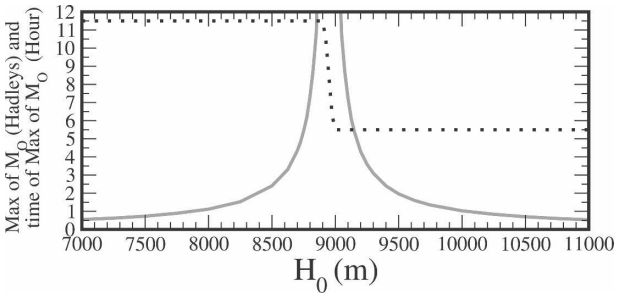

FIG. 11. Semidiurnal mass AAM response in the shallow-water model when $\tilde{X}$ is keyed to the mountain stress $\mathcal{T}$. Sensitivity of the amplitude (thick gray) and phase (dots) of M_O to the value of the equivalent depth H_0 is shown.

shifts by 6 h) when the forcing becomes supercritical (here when $H_0 < 8.9$ km).

d. Baroclinic configuration and diurnal response

If in the same configuration we impose diurnal forcings in the shallow-water model (not shown), the response resembles an $n = 1$ eigensolution of the tidal equations, but its amplitude is very small compared to the corresponding signal from the GCM in Fig. 6. To understand this more precisely, it is necessary to recall that for the diurnal frequency $\sigma/2\Omega = 0.5$ the leading eigenvalues of the Lamb parameters are (from Fig. 1 in LH68)

$$\gamma_1 \approx 25 < \gamma_2 \approx 150 < \gamma_3 \approx 400 < \cdots < \gamma_n < \gamma_{n+1} < \cdots. \tag{25}$$

Hence, the response of the shallow-water model follows that, when $\gamma = 9.8$, the closest eigenvalue of the Lamb parameter is indeed for the gravest mode $\gamma_1 = 25$ but is quite far from it.

To produce more substantial diurnal signals, one needs to consider diurnal forcings imposing a more baroclinic response. In the simplified model [Eqs. (15)–(17)], this can be done by taking for β a pure imaginary value $\beta = i\beta'$ where β' is real. In this case the forcing changes sign at the altitude π/β', it decays more rapidly with altitude than in the barotropic case, and

$$H_0 = \frac{\kappa H}{1/4 + \beta'^2 H^2}$$

can be substantially smaller than before. Although it maintains simplicity, our shallow-water model has in this case an important defect: $\tilde{w}$ is not null at the ground, so the solution in Eq. (14) can only be a part of the forced solution. As we are in a linear framework, we must add to it a solution that is not forced inside the flow, but for which the vertical velocity at the ground opposes $\tilde{w}$. If we neglect it, nearly half ($1–2\kappa = 3/7$ more exactly) of the meridional mass flux associated with the solution in Eq. (14) passes through the lower boundary instead of changing the atmospheric mass $\rho_r \tilde{h}$. This omission has a direct effect on the AAM budget, which can now be written as

$$\frac{d}{dt}\left(M_R + \frac{1}{2\kappa} M_O\right) = T_X, \tag{26}$$

where the wind AAM and the torque due to X are

$$M_R = 2\pi r^3 \int_{-\pi/2}^{+\pi/2} \cos^2\phi \rho_r \frac{H_0}{2\kappa} \tilde{u}\, d\phi,$$

$$T_X = 2\pi r^3 \int_{-\pi/2}^{+\pi/2} \cos^2\phi \rho_r \frac{H_0}{2\kappa} \tilde{X}\, d\phi, \tag{27}$$

while the mass AAM is as in Eq. (21). Its separate budget is given by

$$\frac{d}{dt}\frac{M_O}{2\kappa} = C \tag{28}$$

in which

$$C = -4\pi r^3 \Omega \int_{-\pi/2}^{\pi/2} \cos^2\phi \sin\phi \rho_r \frac{H_0}{2\kappa} \tilde{v}\, d\phi.$$

Again, this AAM budget is very close to the actual AAM budget in Eq. (5): (i) taking for $\mathcal{U}$ in the definition of M_R in Eq. (6) the value $\rho_r(H_0/2\kappa)\tilde{u}$; (ii) taking for $\mathcal{M}$ in the definition of M_O the value $\rho_r \tilde{h}$; (iii) taking for the stresses ($\mathcal{F}$, $\mathcal{T}$, and $\mathcal{B}$) in the definition of the torques in Eq. (7) the value $\rho_r(H_0/2\kappa)\tilde{X}$; and (iv) taking for $\mathcal{V}$ in the definition of the Coriolis conversion term in Eq. (8) the value

$$\rho_r \frac{H_0}{2\kappa} \tilde{v}.$$

1) $H_0 = 2.5$ KM, $n = 1$ RESPONSE TO $\mathcal{T}$

If the first zero of the diurnal forcing in Eq. (13) is near $\pi/\beta' \approx 30$ km, the altitude $H_0 = 2.5$ km, the Lamb parameter $\gamma \approx 35$ is closer to the diurnal value for $\gamma_1 \approx 25$, and the diurnal forcing is supercritical with regard to the $n = 1$ eigensolution. In this case, the response of the shallow-water model when $\tilde{X}$ is keyed to each of the three stresses $\mathcal{T}$, $\mathcal{F}$, and $\mathcal{B}$ is dominated by an $n = 1$ eigensolution of the $s = 0$ Laplace tidal equations. Again, the largest responses are those associated with the mountain stress $\mathcal{T}$ and the angular momentum flux divergence $\mathcal{F}$. It is also for $\mathcal{T}$ that the phase is in better agreement with the LMDz GCM results in Figs. 6a,b. To illustrate this point, Figs. 12a,b show the equatorially antisymmetric patterns for the surface pressure $\rho_r g\tilde{h}$ and for the zonal momentum $\rho_r(H_0/2\kappa)\tilde{u}$ when $\tilde{X}$

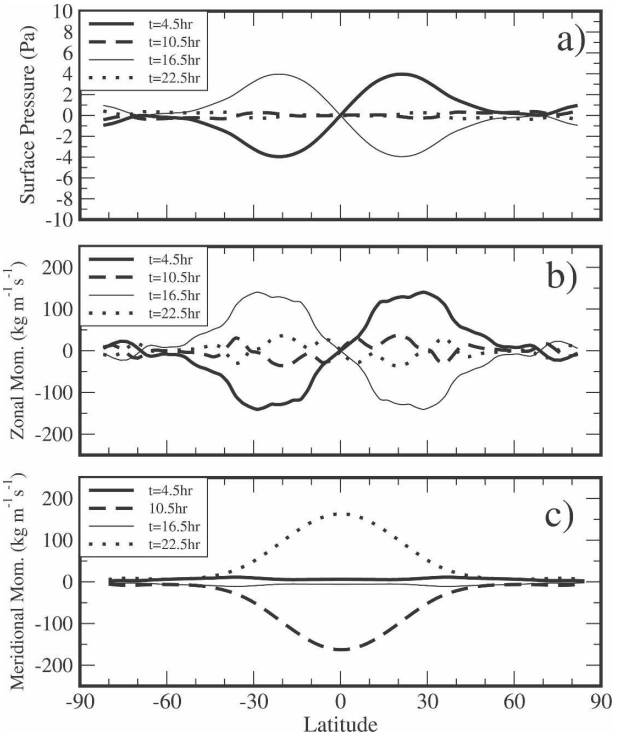

FIG. 12. Diurnal response in the shallow-water model with $H_0 = 2.5$ km and when the forcing $\tilde{X}$ is keyed to the mountain stress $\mathcal{T}$ of (a) the surface pressure (i.e., $\rho_r g\tilde{h}$) pattern antisymmetric with respect to the equator, (b) the zonal momentum [i.e., $\rho_r(H_0/2\kappa)\tilde{u}$] pattern antisymmetric with respect to the equator, and (c) the meridional momentum [i.e., $\rho_r(H_0/2\kappa)\tilde{v}$] pattern symmetric with respect to the equator.

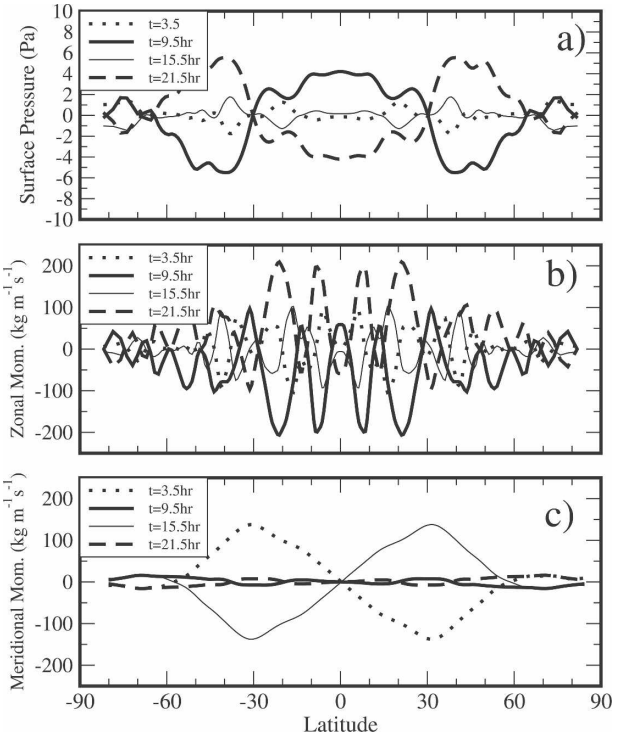

FIG. 13. As in Fig. 12 but with $H_0 = 1$ km and the forcing $\tilde{X}$ keyed to $\mathcal{F}$ for (a) $\rho_r g\tilde{h}$ symmetric, (b) $\rho_r(H_0/2\kappa)\tilde{u}$ symmetric, and (c) $\rho_r(H_0/2\kappa)\tilde{v}$ antisymmetric with respect to the equator.

is keyed to $\mathcal{T}$. Figure 12c shows the equatorially symmetric patterns of the meridional mass flux $\rho_r(H_0/2\kappa)\tilde{v}$

Clearly, for $\rho_r(H_0/2\kappa)\tilde{v}$ in Fig. 12c the agreement with $\mathcal{V}$ from the LMDz GCM in Fig. 6c is quite good both in phase and amplitude. For the zonal wind in Fig. 12b, the resemblance is not as pronounced but stays fairly good; in particular, the location of the jet maxima around $\pm 30°$ is rather well reproduced. Finally, the surface pressure pattern from the shallow-water model in Fig. 12a also has a good shape, but the amplitude is almost half that of the corresponding one in Fig. 6a. This mismatch with the mass fields from the GCM, while the velocity fields compare in amplitude, is again associated with the fact that the forced solution in the shallow-water model only translates 2κ of the meridional mass flux $\rho_r(H_0/2\kappa)\tilde{v}$ into mass $\rho_r\tilde{h}$.

As for the barotropic case, we have also checked that the value for H_0 chosen is not strictly ad hoc, in the sense that it is not the value for which an extremely strong response occurs. Finally, as the shallow-water model response is largely dominated by the antisymmetric responses in mass and zonal wind shown in Figs. 12a,b, it does not present signals in mass and wind AAM tendencies exceeding substantially the diurnal cycle of the total torque T.

2) $H_0 = 1$ KM, $n = 2$ RESPONSE TO $\mathcal{F}$

To produce a diurnal response with amplified signals in mass and wind AAM, we have to consider that a fraction of the diurnal forcing is even more baroclinic than in the previous section. In the shallow-water model, this can be done by considering that the first zero of the forcing is near $\pi/\beta' \approx 17$ km. In this case, $H_0 = 1$ km, $\gamma \approx 90$ is relatively close to $\gamma_2 \approx 150$, and the diurnal forcing is subcritical with regard to the $n = 2$ eigensolution.

In this case, the strongest signal is still obtained when $\tilde{X}$ is keyed to $\mathcal{T}$ and $\mathcal{F}$. To document in one case the structure of the response when the forcing follows the angular momentum flux divergence, Figs. 13a,b show the equatorially symmetric patterns for the surface pressure $\rho_r g\tilde{h}$ and for the zonal momentum $\rho_r(H_0/2\kappa)\tilde{u}$ resulting from the diurnal cycle in $\mathcal{F}$ when $\tilde{X}$ is keyed to $\mathcal{F}$. Figure 13c shows the equatorially antisymmetric patterns of the meridional mass flux $\rho_r(H_0/2\kappa)\tilde{v}$ in the same configuration.

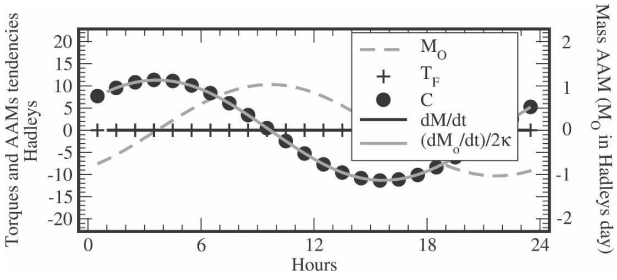

FIG. 14. Diurnal response for the mass AAM budget in the shallow-water model with $H_0 = 1$ km and when the forcing $\tilde{X}$ is keyed to the momentum flux divergence $\mathcal{F}$ of the mass AAM (gray solid), total AAM tendency ($dM/dt = 0$, black solid), mass AAM tendency (here $dM_O/dt/2\kappa$, gray solid), mountain torque ($T_F = 0$, plus symbols), and Coriolis conversion (C, dots).

Again, it is for the meridional mass flux from the shallow-water model [$\rho_r(H_0/2\kappa)\tilde{v}$ in Fig. 13c] that the resemblance with the GCM is the best ($\mathcal{V}$ in Fig. 7c). More specifically, in both models, the two extrema for this quantity are located around ±30°. The comparison between the barotropic zonal winds in the [$\rho_r(H_0/2\kappa)\tilde{u}$ in Fig. 7b and $\mathcal{U}$ in Fig. 13b] is quite difficult, because these fields are rather erratic in both models. This propensity for the momentum flux divergence to produce irregular zonal wind fields was found to be quite systematic (e.g., it does occur for all values of H_0). If related to the diurnal zonal mean budget, the signal for $\mathcal{F}$ exceeds, in some places, the Coriolis force $2\Omega \sin\phi\mathcal{V}$ and is much more irregular [see Eq. (1), Fig. 8b, and the corresponding discussion in section 3c]. This suggests that the irregularities in the zonal wind from the LMDz GCM in Figs. 7b are related to the angular momentum forcing. Finally, the patterns for the surface pressure from the shallow-water model in Fig. 13 also compare relatively well with those from the GCM (once taken into account the 2κ factor on the amplitude discussed above). In particular, the nodes at ±30° are well located. Nevertheless, in the shallow-water model the signal in the polar latitudes is very small, while it is significant in the LMDz GCM. This difference is strongly suggestive that we have decreased H_0 too much to obtain a diurnal signal with realistic amplitude.

It is also of interest to notice that in this baroclinic case the shallow-water solution forced by $\mathcal{F}$ can produce mass AAM variations that compare with those from the GCM. This point is illustrated in Fig. 14, which shows the mass AAM cycle associated with the response displayed in Fig. 13. We see that the mass AAM reaches 1 Hd and is entirely driven by a Coriolis conversion term (C dots) around 10–15 Hd; again one order of magnitude larger than the daily cycle of the torque (Fig. 3b).

5. Conclusions

a. Summary

A 1-yr integration using the LMDz GCM has been performed to analyze the axial angular momentum budget at diurnal and subdiurnal periodicities. The model results have been compared with 12 ECMWF 10-days forecasts and some ECMWF analysis products.

As the surface pressure tides result in longitudinal pressure gradients across major mountain ranges, they give rise to a surface stress $\mathcal{T}$ acting on the zonal mean barotropic flow [Eqs. (1) and (4)]. Globally, this mountain stress results in a mountain torque T_M that has a daily cycle of few hadleys [Eq. (7) and Fig. 1b]. This translates in a daily cycle for the total torque T of the same magnitude, the daily cycle of the boundary layer torque T_B being substantially smaller than that of T_M. The daily cycle of T produces variations in the total angular momentum (M) that are almost one order of magnitude below 1 Hd, that is, very small compared to the amplitude of the natural variations of M. Nevertheless, this very small daily signal in M results, in fact, from the cancellation between much stronger daily cycles of the mass AAM M_O and of the wind AAM M_R (their amplitudes are of a few hadleys, see Fig. 1 for the LMDz GCM and Fig. 2 for the ECMWF forecasts and analysis).

To interpret these large and almost canceling oscillations, we have diagnosed, from the LMDz GCM, the diurnal and semidiurnal cycles of three zonal mean and barotropic fields: $\mathcal{M}$, $\mathcal{U}$, and $\mathcal{V}$, whose latitudinal distributions are directly related to the mass AAM (M_O), the wind AAM (M_R), and the conversion (C) between them, respectively.

The semidiurnal signals in $\mathcal{M}$, $\mathcal{U}$, and $\mathcal{V}$ are almost like the $n = 2$ zonally symmetric ($s = 0$) eigensolution of the Laplace tidal equations. It corresponds to a redistribution of masses ($\mathcal{M}$) from the midlatitude and polar regions toward the equatorial band (Fig. 4a) that results in variations of the mass AAM M_O of a few hadleys (Fig. 3a). It also corresponds to variations in the zonal wind $\mathcal{U}$ with two extrema in midlatitudes of the same sign (Fig. 4b), which results in large variations of the wind AAM M_R. Via conservation of the zonal mean of the atmospheric mass, $\mathcal{M}$ is driven by the transport of meridional mass $\mathcal{V}$ (shown in Fig. 4c), while $\mathcal{U}$ is also driven by $\mathcal{V}$ via the Coriolis torque (because the latter dominates the other forcing terms of the $\mathcal{U}$ tendency in the zonal mean of the zonal momentum budget; see Fig. 5). In terms of the AAM budget, this driving role of $\mathcal{V}$ via the conservation of mass and via the Coriolis force implies that the Coriolis conversion term C is one order

of magnitude larger than the torque T in the separate semidiurnal budgets of M_O and M_R (Fig. 3a).

The diurnal signals in $\mathcal{M}$, $\mathcal{U}$, and $\mathcal{V}$ are more complex to interpret, so we separate, for each field, its symmetric part from its antisymmetric part with respect to the equator.

The equatorially antisymmetric diurnal cycles of $\mathcal{M}$ and $\mathcal{U}$, as well as the equatorially symmetric diurnal cycle of $\mathcal{V}$, are quite substantial and reminiscent of an $n = 1, s = 0$ eigensolution of the Laplace tidal equation. By construction, they cannot be associated with variations in axial mass AAM or wind AAM, and the symmetric part of $\mathcal{V}$ produces no Coriolis conversion between them.

For $\mathcal{M}$, the equatorially symmetric patterns in Fig. 7a also resemble the $n = 2$ zonally symmetric ($s = 0$) eigensolution of the Laplace tidal equations. The same is true for the antisymmetric part of $\mathcal{V}$ in Fig. 7c. Nevertheless, the equatorially symmetric part of $\mathcal{U}$ in Fig. 6b is quite irregular in latitude when compared, for instance, with the symmetric part of $\mathcal{V}$ in Fig. 6c. This follows from the fact that the angular-momentum flux divergence in the right-hand side of the zonal momentum Eq. (1) is as large as the Coriolis term $2\Omega \sin\phi\mathcal{V}$. Nevertheless, and for the same reason as for the semidiurnal signals, these different patterns explain the large but opposite daily cycles in mass and wind AAM (Fig. 3b).

We have then postulated that these large and compensating diurnal and semidiurnal oscillations in M_O and M_R result from a dynamical excitation of axisymmetric free modes of oscillation and that these dynamical forcings are also associated with the surface stresses that affect the zonal-mean angular momentum budget [Eq. (1)]. To support this hypothesis, we have used a shallow-water model driven by dynamical forcings, which vertically integrated equal the various zonal-mean zonal stresses extracted from the LMDz GCM [Eq. (19)].

If the shallow-water model configuration is barotropic (taking for the equivalent depth $H_0 = 9.5$ km), a semidiurnal forcing keyed to the mountain stress induces a response associated with mass and wind AAM oscillations (Fig. 9a) consistent in amplitude and phase with the semidiurnal oscillations seen in the LMDz GCM (Fig. 1c). In the shallow-water model, the response is also dominated by a planetary mode of oscillation very similar to the $n = 2$ and $s = 0$ eigensolution of the Laplace tidal equations (Fig. 10), which is also very near the GCM's results (Fig. 4). These results follow that, in the shallow-water model, the semidiurnal frequency is not far from the eigenfrequency of the $n = 2$ eigensolution. We also find a substantial $n = 2$ response when the shallow-water model forcing is keyed to the angular momentum flux divergence $\mathcal{F}$, but we find a substantially smaller response when it is keyed to the boundary layer stress $\mathcal{B}$. These results stay qualitatively unchanged when we vary the shallow-water model depth, H_0, between 9.2 and 10 km.

To obtain substantial effects at the diurnal frequency in the shallow-water model, we need to consider a more baroclinic setup. For instance, if we take for H_0 a value around $H_0 = 2.5$ km, the diurnal response when the shallow-water model forcing keyed to the mountain stress $\mathcal{T}$ is dominated by a zonally symmetric planetary-scale pattern, which is almost like an $n = 1$ eigensolution of the $s = 0$ Laplace tidal equations (Fig. 12). The shallow-water model response is also close to the zonal mean and barotropic diurnal signal in the LMDz GCM for which the $\mathcal{M}$ and $\mathcal{U}$ patterns are antisymmetric with respect to the equator and $\mathcal{V}$ is symmetric with respect to the equator (Fig. 6). Again the shallow-water model response is comparable when the forcing is keyed to $\mathcal{F}$ but substantially smaller when it is keyed to $\mathcal{B}$. By its $n = 1$ structure, this response from the shallow-water model does not produce amplified signals in mass and wind AAMs.

To produce amplified diurnal signals in mass and wind AAMs in the shallow-water model, one needs to consider an even more baroclinic setup, for instance, taking $H_0 = 1$ km. In this case the response to all stresses is dominated by large-scale circulation patterns resembling the $n = 2$ eigensolution of the Laplace tidal equations. In this case, a good fit with the results from the LMDz GCM in Fig. 7 is found when the forcing is keyed to the divergence of the momentum flux $\mathcal{F}$ (Figs. 13 and 14). The simulation with the shallow-water model nevertheless shows a signal that is rather small at high latitudes compared to the LMDz GCM diurnal signal in Fig. 7. According to the shapes of the eigensolutions in Fig. 7 of LH68, this indicates that we have decreased H_0 too much. Interestingly, the barotropic zonal wind in the shallow-water model response to $\mathcal{F}$ (Fig. 13b) also presents a rather irregular structure. This irregular structure is reminiscent of the one found for $\mathcal{U}$ in the GCM (Fig. 7b), and this illustrates that the divergence of the momentum flux also plays a significant role in our problem.

b. *Significance for geodesy and for the theory of tides*

The results that we presented have two potential domains of application: geodesy and the theory of atmospheric tides.

Concerning geodesy, it is noticeable that nowadays the measurements of the earth orientation parameters

become increasingly precise (Rothacher et al. 2001; Schreiber et al. 2004). Accordingly, analysis of the different terms that affect their diurnal and subdiurnal changes is an important topic of research (Rotacher et al. 2001). To estimate the atmospheric contribution, two methods have been used: the momentum approach and the torque approach. In the first, the AAM of the atmosphere is evaluated directly from atmospheric reanalysis and the earth + ocean angular momentum varies to equilibrate the AAM changes. In the second, the torque of the atmosphere on the earth is evaluated directly from a combination of atmospheric analysis and short-range forecasts. Although the two methods should give exactly the same results, they present large discrepancies at diurnal and subdiurnal periodicities (DeViron et al. 2005). The presence of the large canceling terms between the mass AAM tendency and the wind AAM tendency documented in this paper are probably the origin of these errors for the axial component of the AAM budget.

Still, in the context of geodesy, it is noticeable that our axisymmetric modes exert an axisymmetric pressure force on the earth's surface. In particular, the semidiurnal and the diurnal modes with $n = 2$ can modify the earth's ellipticity at the corresponding periods. For the same reason, the diurnal mode with $n = 1$ can affect the diurnal cycle of the geocenter position along the rotation axis.

Our results also have some implications for the theory of atmospheric tides. In the observations, the diurnal and semidiurnal $s = 0$ tidal signal in surface pressure is close to 10 Pa (Dai and Wang 1999). Although it represents only 10% of the surface pressure tide, this value is not negligible: it corresponds in amplitude to the gravitational (lunar) tide (Goulter 2005). If we assume that the LMDz GCM has a rather realistic diurnal tidal signal and as we reproduce rather well in phase and amplitude the $s = 0$ surface pressure signal with our shallow-water model, we have established here that the dynamical forcings of the zonal mean zonal flow can force a good part of the $s = 0$ surface pressure tide.

Nevertheless, it is quite clear that our reproduction, with a linearized shallow-water model of those axisymmetric and barotropic tidal signals, is not a definite proof that they are due to the forcings analyzed in this paper. To establish this more precisely, a more complete tidal model should be used (see, e.g., Hagan 1996; Hagan and Forbes 2002) and its axisymmetric response to all the possible zonal mean forcings should be analyzed (e.g., dynamical as well as thermodynamical). The latitudinal and vertical structures of these forcings could also be deduced from the GCM, as it has been done here for the latitudinal structures only.

Acknowledgments. The authors thank the three anonymous reviewers for their constructive comments. The numerical calculations for the LMDz GCM were performed using the high performance computational facilities held at IDRIS (France).

REFERENCES

Barnes, R. T. H., R. Hide, A. A. White, and C. A. Wilson, 1983: Atmospheric angular momentum fluctuations, length-of-day changes and polar motion. *Proc. Roy. Soc. London,* **A387,** 31–73.

Chao, B. F., 1984: Interannual length-of-day variation with relation to the Southern Oscillation/El Niño. *Geophys. Res. Lett.,* **11,** 541–544.

Chapman, S., and R. S. Lindzen, 1970: *Atmospheric Tides*. D. Reidel, 200 pp.

Dai, A., and J. Wang, 1999: Diurnal and semidiurnal tides in global surface pressure fields. *J. Atmos. Sci.,* **56,** 3874–3891.

deViron, O., G. Schwarzbaum, F. Lott, and V. Dehan, 2005: Diurnal and subdiurnal effects of the atmosphere on the Earth rotation and geocenter motion. *J. Geophys. Res.,* **110,** B11404, doi:10.1029/2005JB003761.

Egger, J., 2003: Gravity wave drag and global angular momentum: Geostrophic adjustment processes. *Tellus,* **55A,** 419–425.

Frei, Ch., and H. C. Davies, 1993: Anomaly in the Alpine diurnal pressure signal: Observations and theory. *Quart. J. Roy. Meteor. Soc.,* **119,** 1269–1289.

Goulter, S. W., 2005: The structure of the lunar semi-diurnal pressure tide L2. *Quart. J. Roy. Meteor. Soc.,* **131,** 723–758.

Hagan, M. E., 1996: Comparative effects of migrating solar sources on tidal signatures in the middle and upper atmosphere. *J. Geophys. Res.,* **101,** 21 213–21 222.

——, and J. M. Forbes, 2002: Migrating and nonmigrating diurnal tides in the middle and upper atmosphere excited by tropospheric latent heat release. *J. Geophys. Res.,* **107,** 4754, doi:10.1029/2001JD001236.

Hendon, H. H., 1995: Length of day changes associated with the Madden–Julian oscillation. *J. Atmos. Sci.,* **52,** 2373–2383.

Hourdin, F., and Coauthors, 2006: The LMDZ4 general circulation model: Climate performance and sensitivity to parametrized physics with emphasis on tropical convection. *Climate Dyn.,* **27,** 787–813.

Iskenderian, H., and D. A. Salstein, 1998: Regional sources of mountain torque variability and high-frequency fluctuations in atmospheric angular momentum. *Mon. Wea. Rev.,* **126,** 1681–1694.

Lamb, H., 1932: *Hydrodynamics*. 6th ed. Cambridge University Press, 738 pp.

Lejenäs, H., and R. A. Madden, 2000: Mountain torques caused by normal-mode global Rossby waves, and the impact on atmospheric angular momentum. *J. Atmos. Sci.,* **57,** 1045–1051.

Longuet-Higgins, M. S., 1968: The eigenfunctions of Laplace's tidal equations over a sphere. *Philos. Trans. Roy. Soc. London A,* **262,** 511–607.

Lott, F., and F. d'Andrea, 2005: Mass and wind axial angular momentum responses to mountain torques in the 1–25 day

band: Links with the Arctic Oscillation. *Quart. J. Roy. Meteor. Soc.,* **131,** 1483–1500.

——, A. W. Robertson, and M. Ghil, 2001: Mountain torques and atmospheric oscillations. *Geophys. Res. Lett.,* **28,** 1207–1210.

——, ——, and ——, 2004a: Mountain torques and Northern Hemisphere low-frequency variability. Part I: Hemispheric aspects. *J. Atmos. Sci.,* **61,** 1259–1271.

——, ——, and ——, 2004b: Mountain torques and Northern Hemisphere low-frequency variability. Part II: Regional and episodic aspects. *J. Atmos. Sci.,* **61,** 1272–1283.

——, L. Fairhead, F. Hourdin, and P. Levan, 2005a: The stratospheric version of LMDz: Dynamical climatologies, Arctic Oscillation, and impact on the surface climate. *Climate Dyn.,* **25,** 851–868.

——, L. Goudard, and A. Martin, 2005b: Links between the mountain torque and the Arctic Oscillation in the Laboratoire de Météorologie Dynamique (LMDz) general circulation model. *J. Geophys. Res.,* **110,** D22107, doi:10.1029/2005JD006073.

Madden, R. A., 1987: Relationship between changes in the length of day and the 40- to 50-day oscillation in the Tropics. *J. Geophys. Res.,* **92,** 8391–8399.

Rothacher, M., G. Beutler, R. Weber, and J. Hefty, 2001: High-frequency variations in Earth rotation from Global Positioning System data. *J. Geophys. Res.,* **106,** 13 711–13 738.

Schreiber, K. U., A. Velikoseltsev, M. Rothacher, T. Klügel, G. E. Stedman, and D. L. Wiltshire, 2004: Direct measurement of diurnal polar motion by ring laser gyroscopes. *J. Geophys. Res.,* **109,** B06405, doi:10.1029/2003JB002803.

Tanaka, H. L., and A. Kasahara, 1992: On the normal modes of Laplace's tidal equations for zonal wavenumber zero. *Tellus,* **44A,** 18–32.

Thompson, D. W., and J. M. Wallace, 1998: The Arctic Oscillation signature in the wintertime geopotential height and temperature fields. *Geophys. Res. Lett.,* **25,** 1297–1300.

von Storch, J.-S., 1999: The reddest atmospheric modes and the forcing of the spectra of these modes. *J. Atmos. Sci.,* **56,** 1614–1626.

——, 2001: How do friction and pressure torques affect the relative Ω angular momenta of the atmosphere. *J. Atmos. Sci.,* **58,** 1995–1999.

Weickmann, K. M., G. N. Kiladis, and P. D. Sardeshmukh, 1997: The dynamics of intraseasonal atmospheric angular momentum oscillations. *J. Atmos. Sci.,* **54,** 1445–1461.